Structural modification enhances the optoelectronic properties of defect blue phosphorene thin films

M.T. Dang[1*], N.V.A. Duy[2], A. Zaccone[3], P. Schall[4], V.A. Dinh[5]

[1]*School of Education, Can Tho University, 3/2 St., Ninh Kieu Dist., Can Tho, Vietnam*
[2]*FPT University, CanTho campus, 600 Nguyen Van Cu street, Ninh Kieu, Can Tho, Viet Nam*
[3]*Department of Physics "A. Pontremoli", University of Milan, via Celoria 16, 20133 Milan, Italy*
[4]*Van der Waals-Zeeman Institute, University of Amsterdam, Science Park 904, Amsterdam, The Netherlands*
[5]*Department of Precision Engineering, Graduate School of Engineering, Osaka University, 2-1 Yamadaoka, Suita, Osaka 565-0871, Japan*

*Corresponding author: Minh Triet Dang dmtriet@ctu.edu.vn

Abstract: Active enhancement of the optical absorption coefficient to improve the light converting efficiency of thin-film solar cell materials is crucial to develop the next-generation solar cell devices. Here we report first-principles calculations with generalized gradient approximation to study the optoelectronic properties of pristine and divacancy blue phosphorene thin films under structural deformation. We show that instead of forming sp-like covalent bonds as in the pristine blue phosphorene layer, a divacancy introduces two particular dangling bonds between the voids. The orbital hybridization of these dangling bonds is strongly modified in both the velocity and vorticity directions depending on the type of deformation, creating an effective light trap to enhance the material absorption efficiency. Furthermore, this successful light trap is complemented by a clear signature of $\sigma + \pi$ plasmon when a divacancy blue phosphorene layer is slightly compressive. These results demonstrate a practical approach to tailor the optoelectronic properties of low dimensional materials and to pave a novel strategy to design functionalized solar cell devices from the bottom-up with selective defects.

Keywords: blue phosphorene, first-principles, deformation, optoelectronic properties

Recent advances in material synthesis allow the fabrication of low-dimensional materials with controllable optoelectronic properties from the bottom-up approach in a more effective way [1]–[3]. First introduced in 2004 by Geim and Novoselov, graphene, a typical low-dimensional material, has rapidly received attention by the physical community thanks to its attractive mechanical and optoelectronic material properties [4]. Graphene was believed to replace the standard silicon dioxide to pave a novel revolution in semiconductor industry. However, since graphene is a gapless material, the integration of graphene layers to current chip technology is strongly limited. Recently, we have experienced a new zoo of theoretical as well as experimental reports to propose a next generation of graphene-like materials such as two-dimensional layers of boron nitride [5], MoS_2 [6], silicene [7], and many more metal-dichalchogenides [8] … In 2014, black phosphorene was successfully discovered from scotch-tape-based microcleavage of the layered bulk black phosphorous and MoS_2 [9] and was predicted to greatly contribute to the development of the next generation of field effect transistors (FET) and other optical devices [10], [11]. Furthermore, besides the explored black phosphorene, thanks to the support of molecular dynamics simulations, physicists also predicted other interesting morphologies of phosphorene [12], [13] and blue phosphorene stands out as the most stable phase of phosphorus [14], [15]. In 2016, Chen and his co-workers succeeded in growing a single layer of blue phosphorene (BlueP) on Au(111) [16], [17] using a molecular beam epitaxial crystal growth technique and predicted a new development of novel optoelectronic devices together with embedded blue phosphorene layers [18]–[21].

Two-dimensional layered materials such as graphene, MoS_2, and phosphorene exhibit remarkable mechanical flexibility, in which the materials can sustain a tensile strain above 25% [22]–[24]. This spectacular mechanical property, originating from the inherent puckered (buckled) surface formed by the sp^3 hybridizied tetra-phosphorus, opens increasing applications in advanced material science and engineering [25]. Thanks to the long-range correlation of the lattice point symmetry, the elastic deformation of defect-free 2D structures before yielding is mainly driven by the local balance of forces induced by affine displacements. In an elastic regime, the material can easily find lower free-energy minima to stabilize the complex networks. Once the material has a defect site, under shear, the material would drive into non-affine atomic displacements, however, a generic picture to capture simultaneously the free energy landscape and particle displacements for 2D materials under flow is still lacking. Disentangling the complex contributions of affine and non-affine displacements and connecting them to the free energy landscape of 2D thin films remain a crucial challenge. Recently, Ghaffari, et. al. [26] proposed a hyperelastic membrane material model to describe the mechanical responses of a defect-free single layer BlueP sheet under small deformations in the elastic regime. Based on a set of invariants, this model successfully captures the anisotropy of linear elasticity constants when a BlueP thin film is deformed or under indentation. However, this set of invariants is difficult to address experimentally.

Under deformation, it is well-accepted that the broken symmetry of perfect sp^3 hybridization of tetra-phosphorus leads to significant modification of the atomic bonding orientation, and related change of the materials' band gap. So far, the most successful model to interpret the change of the electronic band gap inducing a semiconductor-metal transition of black phosphorene was proposed by Rodin, et. al. [27]. The authors analyzed the localized orbital compositions obtained from tight-binding models to uncover the underlying σ and π bonding between the neighboring orbitals under compression. In an extreme maximum puckering case, the vertical shifts resulting from the antisymmetric aligned neighboring p_z orbitals at the valance band maximum (VBM) and the symmetric p_z orientation at the conduction band minimum (CBM) lead to a gap reduction and eventually induces band crossing. Peng et. al. [24] consolidate this finding from electron-electron and electron-ion interaction analyses: the authors proposed that during tensile strain, the energy created by the electron-ion interaction increases faster than the reduction of the electron-electron one, resulting in an increase of bonding and decrease of antibonding energy. Albeit these hypotheses succeeded in explaining the electronic changes of black phosphorene under shear, the effect of directional bond orientations on the onset of flow of blue phosphorene remains incomplete.

In this paper, we report first-principles calculations with generalized gradient approximation to study the optoelectronic properties of pristine and divacancy blue phosphorene thin films under deformation. We propose a theoretical framework based on strain-induced forces that balance by symmetry in centrosymmetric crystals with additional non-affine displacements to connect the shear-induced microscopic structure to the macroscopic free energy of deformation and calculate the resulting elasticity constants. We demonstrate that under shear, the orbital interactions are manifested essentially in the compression and extension axes, resulting in a modification of the electronic band gap. In the presence of a divacancy, this broken symmetry introduces two particular dangling bonds between the voids and becomes a light trap with a clear $\sigma + \pi$ plasmon signature, thus enhancing the material absorption efficiency. These results demonstrate a practical approach to tailor the optoelectronic properties of low-dimensional materials and a novel strategy to design functionalized solar cell devices with significant increase of absorption coefficient from the bottom-up using selective defects.

Results

Mechanical responses of BlueP thin films under deformation. To explore the effect of structural modification on the mechanical responses of BlueP thin films, we performed DFT optimization to obtain the two most stable configurations of pristine and DV BlueP as shown in Fig. 1. The primitive unit cell of the optimized BlueP is a hexagonal lattice with a space group of D_{3d}^3, which is in excellent agreement with previous work [28], [29]. The lattice constant (a), the P-P bond length (d), the buckling height (h) between the upper and the lower layer P atoms, and the bond angle (θ)

of this primitive cell are a=3.32 Å, d=2.284 Å, h=1.24 Å, and $\theta = 94.84^0$, respectively, in quantitative agreement with refs. [11], [30]. As discussed in refs. [10], [31], [32], there are several ways to introduce a vacancy to a BlueP thin film. We decided to replace the 15th and 16th P atoms with a vacancy to obtain the optimized *divacancy* configuration in Fig. 1d. Our choice of eliminating these two P atoms is to maximize the possibility to create dangling bonds between the 3rd and 13th P atoms and between the 6th and 10th P atoms. Dangling bonds are obviously weaker than covalent bonds so the mid-gap states created by these dangling bonds can significantly increase the number of energy states in the absorber material. This technique is equivalent to an introduction of additional optical traps to enhance the solar energy harvesting efficiency [33]. The formation energy of this particular DV system is about 3.37 eV, which is in a reasonable formation energy range reported by refs. [31], [34]. Table S1 and S2 present the bond lengths between the labelled P atoms of the optimized defect-free and DV BlueP systems. It is obvious that the decrease of bond lengths between P atoms around the defective site illustrates that after geometrical optimization, the P atoms rearrange in such a way to minimize the size of the defect void.

We now impose an external strain to the material by stretching or compressing the lattice in the a-direction while fixing the lattice in the perpendicular direction to employ uniaxial deformation as suggested in [26]. Note that using a fundamentally similar approach, we could resolve the small but distinct structural modification of amorphous materials under shear using confocal microscopy [35], [36] and X-ray scattering [37], [38]. Figs. 1b and 1e present the atomic distances between selected P atoms as a function of strain. Obviously, a linear increase of atomic distances under strain clearly indicates that the deformation of pristine BlueP is mainly composed by affine deformation. However, the non-monotonic behavior of DV BlueP's atomic distances reveals reminiscence of a non-affine contribution. To link the structural modification to the thermodynamic properties of the thin films, we determine the free energy density difference as $\frac{\Delta F}{V} \equiv \frac{1}{V}(F(\gamma) - F(0))$, which is the difference between the free energy density of the deformed states and the free energy of the unstrained states at rest. As discussed in the **Methods** section, this quantity encodes the local affine, non-affine distortions as well as the irreversible rearrangements due to thermodynamic relaxation. We plot the calculated free energy densities of pristine and DV BlueP in Figs. 1c and 1f, respectively. To quantify the affine, non-affine and dissipated energy contributions of the 2D materials under strain, we fit the free energy density difference data using eq. 3 to obtain the resulting Young's (κ) and shear modulus (G_R). Following ref. [26], we then compute the bulk modulus $G = \frac{\kappa G_R}{4G_R - \kappa}$ and Poission's ratio $\nu = \frac{G - G_R}{G + G_R}$ as presented in Table 1. Our calculated elastic constants of pristine BlueP using a simple affine-non-affine microscopic model show excellent agreement with the results obtained from a more sophisticated hyperelastic membrane material model [26]. Furthermore, the obtained fitting parameters of A=2.383 and a zero B, as discussed in the **Methods** section, clearly mark the crucial role of affine deformation in pristine BlueP.

We now extend our microscopic model to calculate the elastic constants of DV BlueP thin films, values included in Table 1. This is for the first time that such elastic constants of a defective system are calculated using a first-principle method. Obviously, in the presence of a defect void, the elastic constants of this material are slightly weaker than those of the bare system. However, the close match of Poisson's ratio between the two cases remind of identical morphological effects of these two materials. The sign change of the fitting parameter A to -3.987 and a small value of B of 0.373 suggest the formation of weak dangling (covalent) bonds under shear (as shown in Fig. S4), which will be discussed in detail in the next subsection.

Electronic band structure modification under deformation. Active control of the electronic band gap is crucial in designing materials for applications in electronic and optoelectronic devices. Here we investigate the effect of compressive and tensile uniaxial strains on the electronic properties of pristine and DV BlueP.

Without applied strain (Fig. 2c), pristine BlueP has an *indirect* bandgap of 1.94 eV, obtained by the difference between the VBM and CBM states as indicated by red arrows, with the VBM

along the Γ-K region and the CBM along the Γ-M line, showing excellent agreement with previous reports [30], [31], [39]. We also observe a second valence band edge along the Γ-M region with ~10 meV lower than the VBM state, which is in line with [30]. We further explore the electronic origin of these band dispersions by evaluating atomic orbital characteristics of these systems via the total and projected density of states (TDOS and pDOS), and crystal orbital Hamilton population (COHP). While the TDOS and pDOS provide a clear picture about orbital composition, the COHP analyses provide insights into the nature of the bonds: positive and negative values of COHP indicate bonding and anti-bonding states, respectively. As shown in Fig. S1b, both the valence and conduction bands of pristine BlueP are mainly formed by symmetrical up-down p orbitals [*I will update Fig. S1b in the next version*], suggesting that the pristine BlueP at rest is a non-magnetic material. Focusing on orbital interactions at specific bonds, we consider tetrahedron configurations, i.e. a tetrahedron composed by an out-of-plane P15 and three in-plane P3, P13, P16 atoms (Fig. 1a). In terms of directional orientations, the p_y orbital orientates along the b-axis whereas the p_x orbital is perpendicular to the b-axis (Figs. 4c-d). The p_z component (c-axis) plays a major role in the hybridization mechanism due to the unique tetrahedron symmetry of P atoms in the BlueP layer. Figures 2g and S1e reveal that the VBM is dominated by 3s-3p_z σ bond while the CBM are predominated by 3s-3p_x and 3p_x-3p_y σ and 3p_x-3p_z π bonds. The antisymmetric 3p_z-3p_z π antibond together with other bonding states demonstrate that even for a defect-free BlueP, this buckling material inherits highly anisotropic directional bond orientations which leads to complex orbital interactions under deformation.

In the presence of a local defect, Fig. 3c demonstrates that the introduction of a divacancy does not change the intrinsic electronic property of BlueP materials except narrowing down the indirect band gap to 0.74 eV in qualitative agreement with [31], [39]. Analogous to the pristine BlueP, the DV BlueP also shows a symmetrical behavior of TDOS (Fig. S3c) indicating that the strain-free DV system is a non-magnetic semiconductor. In contrast to the band structures of the pristine BlueP, we observe the existence of two localized mid-gap bands in the conduction band. By evaluating all orbital interactions of P atoms, we identify that the two localized mid-gap states are caused by the P3-P13 and P6-P10 dangling bonds (as illustrated in Figs. 3g and S3c for P3-P13 pCOHP analysis). It is apparent that the VBM is mainly contributed by 3s-3p_y σ and 3p_z-3p_z π orbitals while the localized impurities of P3-P13 and P6-P10 are dominated by 3p_x-3p_y σ orbitals and 3p_z-3p_z and 3p_y-3p_y π orbitals in the conduction band. These analyses highlight the essential role of orbital directional orientations and envisage the strong effect of structural modification on the electronic properties of these materials under shear.

Now, we evaluate the effect of the shear on defect-free BlueP thin films. Figures 2a-e demonstrate that the band structures of compressed pristine BlueP are more sensitive to structural modifications than those of tensile systems: the band gap decreases more rapidly under compressive strain and even exhibits semiconductor-metal transition when the level of compression exceeds 10% strain. Also, the VBM shifts to the Γ point while the CBM remains in the Γ-K region when the material is compressed. Nevertheless, when pristine BlueP is stretched along the a-axis, the VBM shifts to the K point whereas the CBM shifts to the Γ point. Considering the actual values of these electronic states, we notice that albeit the CBM shows slight downshifts from -1.09eV (strain-free, 0%) to -1.93eV (+8% tensile strain) and to -1.31eV (-8% compressive strain), and the VBM exhibits a striking difference between the two deformation mechanisms: a minute upward shift from -3.16eV (0% strain) to -3.08eV (+8%) versus a remarkable upshift to -1.71eV (-8% strain). Furthermore, comparing Fig. 2g with Fig. 2h, we conceive that the uniaxial tensile strain manifests the 3p_z-3p_y π bonding orbital at the CBM as well as the 3p_x-3p_z π antibond orbital at the VBM. More interestingly, when the pristine BlueP is compressed up to -8% strain, the valence band exhibits a remarkable change: the antisymmetric 3p_x-3p_x and 3p_x-3p_y states shift the valence band up towards the Fermi level and relatively 1eV above the maximum energy of the s-p bonds. The resulting antisymmetric states give rise to the sharp increase of band curvatures along the Γ-K and Γ-M regions in Figs. 2a-b and clearly mark the highly directional anisotropy of band structures under compression.

4

The electronic properties of the DV systems under deformation differ significantly. As illustrated by undistinguishable up and down band curves in Fig. 2a-c and symmetrical up and down DOS in Fig. S3a-c, the DV system does not exhibit magnetic properties under compression. The corresponding band gaps slightly increase from 0.74eV (strain-free) to ~0.97eV at -8% strain. When compression is applied, the hybridization between the bonding orbitals of P3 and P13 (and P6-P10) becomes stronger, the COHP is more localized as shown in COHP Figs. S3a-b, resulting in the formation of dangling bonds. As also observed in Figs. S3a-b and Figs. S4a-b, the formation of weak dangling bonds between P3-P13 and P6-P10 at -4% strain and the new covalent bond at -8% strain makes all electrons saturated so the compressed DV systems are non-magnetic. This argument is consolidated by the sign change of the A fitting parameter in the previous subsection. In contrast to the compressed DV systems, when DV systems are uniaxially tensiled, the hybridizations of bonding orbitals of the above-mentioned P atoms are significantly weaker (as demonstrated by the decrease of the COHP amplitudes in the conduction bands in Figs. S3c-e), the COHP becomes delocalized and hence their unpaired electrons cause the spin polarization as the tensile is strong enough. Consequently, these systems would become magnetic when a sufficient tensile strain is applied. In our calculation, at +8% tensile strain, the system becomes strongly spin-hybridized with a magnetic moment of 4μB.

Why are the directional bond orientations strengthened in certain directions? How do these changes relate to structural modifications? To address this, we attempt to use our simple distortion model of nearest-neighbors to provide insights into the effect of the shear on the electronic properties of this material. Recall that for a black phosphorene sheet under compression, Rodin, et. al. [27], via a tight-binding model, pointed out that the upshifted energy level originates from the symmetrical alignment of the neighboring $3p_z$ components along the c-axis: to be precise, symmetrically aligned neighboring p_z orbitals may form an antibonding σ bond and vice versa; however, if the σ bond energy is greatly larger than that of the π bond, the generic bond nature is reversed. Albeit the proposed mechanism partly interprets the upward energy shift of the valence band under compression, the underlying mechanism behind the effect of compression on directional bond orientations is still incomplete. Here, we extend Rodin, et. al.'s model as follows. When a pristine BlueP is tensile along the a-direction (Fig. 4c), in the velocity-velocity gradient plane, the material shows a real-space contraction in the p_y-direction and dilation in the p_x-axis. If a pristine BlueP is compressed in the a-axis, the real-space contraction and dilation directions are reversal (Fig. 4d). In case the energy of π orbitals is larger than that of the σ orbitals, the compression mechanism results in more bonding states while the dilation response leads to more antibonding energy. However, if the σ bond is sufficiently stronger than the π bond, a compressed bond induces a phenomenon antibonding σ bond instead of a bonding one and vice versa. We verify our model for both defect-free and DV BlueP systems by simultaneously evaluating the COHP analyses of P15-P3 bonds under shear. When a pristine BlueP is tensiled at +8% strain, Fig. 2h shows that the newly formed 3pz-3py bonding state originates from compressed atomic bonds along the $3p_y$ axis, and the dominated antibonding $3p_z$-$3p_z$ orbitals is caused by the dilation along the $3p_x$ axis. In the opposite case, at -8% compressed strain, the valence band is mainly contributed by the σ bond, the compression along the $3p_x$ axis causes highly energetic antibonding $3p_x$-$3p_x$, leading to gap reduction. With regard to the DV BlueP systems under strain, by evaluating the orbital interactions between P3-P13 dangling bonds, we also observe the more favorable interactions between P3 ($3p_y$) and P13 ($3p_x$) σ orbitals at the VBM when the DV BlueP is compressed and between $3p_z$-$3p_z$ π orbitals when this material is under a tensile strain.

Structural modification enhances optical properties. We now evaluate the optical responses of pristine and DV BlueP under deformation with an incident electric field parallel to the BlueP surface. As presented in the **Methods** section, one can describe the absorption of a material as a result of direct transitions from the occupied to the empty electron states via the complex dielectric functions. Figures 5a and 5b illustrate the imaginary parts ε_2 of these complex functions for both pristine and DV BlueP. In combination with Fig. S6, it is obvious that the first absorption peaks of

the imaginary part ε_2 quantitatively correspond to the direct transitions from the two most favorable bonding states defined by the COHP analyses in the conduction and valance bands: for instance, the peak at 1.7 eV at -8% compressive strain of the pristine BlueP in Fig. 5a is composed by a direct transition from the first COHP peak at 0.5 eV in the conduction band to the most dominant COHP peak at -1.4 eV in the valence band; and also the absorption peak at 0.4 eV of the DV BlueP under +4% tensile is contributed by a transition from the first peak of the COHP spectra in the conduction band at 0.4 eV to its VBM state. More interestingly, the strong hybridization of the p orbitals of the pristine BlueP layer under deformation signifies a remarkable optical improvement of the imaginary dielectric function ε_2 in the low-energy regions (Fig. 5a, inset). This interesting observation is more pronounced when deforming a DV BlueP thin film, which demonstrates that the optical properties of DV systems are more energetically sensitive to structural deformation. While the band gaps of the materials under deformation are reduced and even vanish with increasing strain, the first absorption peaks of the imaginary parts ε_2 of the pristine and DV BlueP show two interesting trends: for DV systems, elongated to the compression direction, these peaks shift towards the higher energies and the intensity decreases in the same manner. However, for pristine systems, in the same compression line, a red shift of the first peaks of ε_2 is observed as applying the strains up to +8% from the unstrained system, and the red shift would also occur if the unstrained system is compressed up to -8% strain. As shown in Fig. 5, the intensity of the imaginary part ε_2 is highest for the unstrained structures over the entire investigated light excitation energy range; however, in the low energy regime (Fig. 5b), the equivalent quantity of the +8% tensile DV BlueP structure dominates, as a result of the strong covalent bond interaction between the 3rd and 4th magnetized P atoms (Fig. S3). This result emphasizes the role of the localized charge accumulation in the tensile structures and also indicates the possibility of using DV BlueP materials for low-energy optoelectronic devices.

While the main peaks of imaginary parts of the complex dielectric function can be deduced from the most dominant peaks of COHP spectra, the static dielectric constant, obtained from the real part of the dielectric function at zero photon frequency, provides useful information about distinct plasmonic excitations of the materials under deformation. Figures S5 and S6 illustrate the real parts and the module the complex dielectric function while the static dielectric constant ε_S under shear is given in Table 2. Under deformation, the static dielectric constant of the pristine systems remains almost constant around ~3.00 while this corresponding quantity of the defect DV cases almost doubles from 2.95 to 5.78 when the material is tensile to +8% strain. Recall that the band gaps of pristine and DV BlueP decrease significantly with increasing strains, and DV systems are even magnitized when the level of tensile above +8% strain (Fig. S4). We further explore this striking behavior by examining the relation between the static dielectric constant and the band gaps via the well-known Penn's model expression [40]. Penn pointed out that for small wave-number dependent dielectric functions, Umklapp processes play an essential role to the dielectric function and the electronic band gap of semiconductor (E_g) can be approximately related to the static dielectric constant as $\varepsilon_S \approx 1 + \frac{E_P}{E_g}$ [40], where E_P is the optical plasmonic energy gap. Using this expression, we calculated the optical plasmonic energy gaps, and directly compared with the first major peaks of the complex dielectric spectra in the low-energy regime in Fig. S5. Table 2 shows an excellent agreement between the plasmonic peaks calculated from these techniques for pristine systems in most cases. However, in the case of DV systems, these two methods only show qualitative agreement, particularly in the extreme low energy-regime. This large discrepancy may suggest a better theoretical model in combination of local distortion mechanism and optical responses.

At small wave numbers, we succeed in using Penn's model to interpret the plasmonic energy gaps obtained from the complex dielectric function and directly connect these peaks to the electronic band gaps of pristine and DV BlueP under deformation. However, the local maxima in the middle energy range (around 4.0 eV) and the local minima around 8.0 eV suggest a signature of electron excitations known as plasmons. To quantify the plasmon behavior of these pristine and DV BlueP under strains, we calculated the electron energy loss spectra (EELS) [39]. In Figures 5c and

5d, the sharp peaks of the high energy $\pi + \sigma$ plasmons above 8.0 eV are associated with weak π and strong σ electrons while the broad peaks in the middle energy range are originated by weak π excitations. This observation is in line with the plasmonic features presented in [39] for ultra-narrow pristine BlueP nanoribbons under uniaxial strains. More interestingly, the amplitude of the EEL peaks for high energy plasmons of pristine BlueP thin films is about 6 times higher than the corresponding quantities calculated from BlueP nanoribbons [39], indicating the possibility of using pristine BlueP thin films for plasmon solar cell devices. Under deformation in the *a*-direction, the EEL peaks of the high energy plasmons are prominently red-shifted with increasing strains. When introducing DV defects to BlueP thin films, the materials show non-monotonic EEL behavior for both low and high energy plasmons; nevertheless, the strength of the EEL intensity is still doubled the reported EEL intensity calculated from BlueP nanoribbons [39]. These results promise a novel way for using BlueP thin films as prospective plasmon-enhanced solar cells.

We further explore the optical properties of these interesting materials by calculating the refractive index (Fig. S7), the reflectivity (Fig. S8) and the absorption coefficient (Fig. S9) using the particle approximation for linear optical response functions [41]. We also present the refractive index and reflectivity at zero frequency in Table 1. In general, the refractive index of pristine and DV BlueP does not alter much under strains in the visible light spectra but decreases significantly in the upper energy regime. Remarkably, when being stressed out, the DV systems are magnetized, causing a sudden increase of the refractive index in the low energy photon limit. Reflectivity, an indication of the amount of photons being reflected from the material, is considerably low (below 20%) in the visible light range, illustrating that these BlueP thin films can be used as antireflective coating material for solar panels. To demonstrate the high applicability of BlueP thin films for solar cell devices, we plot the absorption coefficient spectra of these materials in the range of 350-750nm, which is identical to the sunlight illumination at sea level. It is obvious that BlueP thin films can absorb sensitively close to the ultra-violet regime, in which a small structural deformation of the materials could lead to a noticable increase of absorption coefficient. While the absorption coefficient of pristine BlueP in the compressive states completely dominate over the whole selected photon emission range, this quantity is slightly higher in the tensile direction when being excited by red light. In the case of DV systems, the absorption of the -8% compressive material dominates the entire selected light range. The calculated absorption coefficient demonstrates that pristine and DV BlueP under a small compression can enhance the absorption capacity of the materials in the visible light range, constituting the material applicability to photovoltaic devices.

Conclusion

In summary, we have successfully applied DFT calculations to systematically investigate the optoelectronic properties of divacancy BlueP under minute structural deformation. We have found that pristine BlueP significantly decreases its electronic band gaps in both ways of deformation while our selected DV BlueP shows a slight increase of band gap when the material is compressive. Furthermore, our results suggest that the absorption capacity of defect BlueP under deformation is enhanced prominently when the material is slightly compressive, which originates from the dangling bonds in the material when the spatial distances between the P atoms are short enough or when the P atoms are magnetized under tensile strain. The presence of $\sigma + \pi$ plasmons also creates additional light traps to improve the light to electricity conversion efficiency of these defect BlueP thin films. These results indicate that selective DV BlueP can be considered as a promising candidate for next-generation solar cell devices.

Methods

Framework of (non-)affine deformation of a two-dimensional thin film. We propose a theoretical framework to describe the mechanical responses of a defective BlueP thin film under deformation. To capture the classical free energy density, we assume the free-standing BlueP thin

film is charge stabilized with an interlayer distance (d_0) of d_0=5.272 Å governed by van der Waals interaction as reported in [42].

Consider a perfect two-dimensional BlueP sheet composed of phosphorus (P) atoms. The deformation of a BlueP thin film is composed of three main components: First, the affine displacements are defined as $\boldsymbol{u}_{ij}^A = \boldsymbol{r}_{ij}^A - \boldsymbol{R}_{ij}^A = \boldsymbol{\gamma} \cdot \boldsymbol{R}_{ij}^A$, where $\boldsymbol{\gamma}$ is the macroscopic strain tensor and $\boldsymbol{R}_{ij}$ the equilibrium covalent bond vector in the undeformed state. In a linear elastic deformation, the net force acting on a P atom is cancelled by symmetry and the P atoms are equilibrated at the lattice points. The resulting free energy density of affine deformation is defined as [36], [43]

$$\frac{\Delta F_A}{V} = \frac{1}{5\pi} \frac{\kappa}{R_0} \frac{NV_0}{V} [n_b^0 \exp(-A\gamma)]\gamma^2 \qquad (1)$$

where κ is a Young's modulus; R_0, N, V are the equilibrium average covalent bond length, the total number of P atoms and the total volume of the BlueP system, respectively, in a supercell lattice; V_0 is the volume of a P atom, n_b^0 is the average coordination number at zero strain. Under deformation, the lattice distortion may break up certain bonds or introduce new-born bonds to the P network. To capture the "birth" or "death" of bonds under shear, we assume the local cage dynamics is governed by the Smoluchowski equation with strain [44] and we model this behavior via an exponential expression of $n_b^0 \exp(-A\gamma)$ where A is a fitting parameter. A positive value of A means that the system mainly breaks its bonds under shear while a negative value indicates that new bonds are formed during deformation. For greater detail of this expression, we refer to refs. [36], [45], [46].

In the presence of a defective site, the non-zero net force acting on a P atom i from its nearest-neighbors has to be balanced by a non-affine deformation to preserve the mechanical equilibrium (Fig. 5b). The non-affine motion brings the P atom to the non-affine position $\boldsymbol{r}_i^{NA}$, and the work associated with the non-affine displacement $\boldsymbol{u}_i^{NA} = \boldsymbol{r}_i^{NA} - \boldsymbol{r}_i^A$ is equal to the work W required to bring the P atom i from the non-affine position back to the affine position as $W \propto \boldsymbol{u}_i^{NA} \cdot \boldsymbol{u}_i^{NA}$ ==(add citation here to Zaccone Mod. Phys. Lett. B 2013)==. Thus, the total free energy of the elastic deformation is

$$\frac{\Delta F_A}{V} = \frac{1}{5\pi} \frac{\kappa}{R_0} \frac{NV_0}{V} [n_b^0 \exp(-A\gamma) - B]\gamma^2 \qquad (2)$$

where B is a fitting parameter representing the strength of bonds in the deformed state. Note that, if the interactions between all P atoms in a BlueP thin film are covalent bonds, the fitting parameter B should be close to 2.4 [47]. Also, a fitting value lower than 2.4 indicates that a mechanically unstable configuration is generated under shear.

The deformation of a defective solid also involves irreversible rearrangements. The dissipated energy associated with continuously ramping the strain at certain strain rate $\dot{\gamma}$ is $W_{diss} = \int_0^t \sigma(s)\dot{\gamma}ds$, where the stress $\sigma(t) = \dot{\gamma} \int_0^t G(s)ds$ [48] with G(t) the strain-dependent relaxation modulus. For a standard linear viscoelastic solid at a very low strain rate, the dissipated energy can be expressed as $W_{diss} \approx \frac{1}{2}G_R\gamma^2$, where G_R is the shear modulus of the defective material. Having specified all free energy contributions, the total free energy of defective BlueP under deformation can be expressed as

$$\frac{\Delta F}{V} = \frac{1}{5\pi} \frac{\kappa}{R_0} \frac{NV_0}{V} [n_b^0 \exp(-A\gamma) - B]\gamma^2 - \frac{1}{2}G_R\gamma^2 \qquad (3)$$

Computational methods. All density functional theory (DFT) simulations are performed using the Projector Augmented Wave (PAW) method implemented in the Vienna *Ab initio* Simulation Package (VASP) [49]–[51]. We used the generalized gradient approximation of the Perdew-Burke-Ernzerhof (PBE) functional [52] as an exchange-correlation functional. The integration in the Brillouin zone was employed using the Monkhorst-Pack scheme[53] (5×5×1) with an energy cut-off of 500 eV. The convergence threshold for the self-consistent field calculations was set to 10^{-5} eV per cell, and the geometrical structures were fully optimzed until the Hellmann-Feynman forces

acting on atoms were less than 0.01 eV/Å. To avoid the atom interactions between the imaged periodic phosphorene thin films, a vacuum of 20 Å thickness was employed between the neighboring phosphorene layers. In the case of divacancy (DV) systems, we introduced spin polarizations to our electronic anlyses.

The formation energy to evaluate the stability of the divacancy optimized configuration with respect to the defect-free system at zero strain is defined as $\Delta E = E_{DV} - E_{ideal} - N\mu_P$, where E_{DV} and E_{ideal} are the total free energy of DV and pristine BlueP, respectively, N is the number of P atoms eliminated in the DV structure which is equal to 2 in this case, and μ_P is the chemical potential of a phosphorus atom.

Strain deformation in our BlueP systems is applied along the *a*-axis (Fig. 1). The magnitude of strain γ is defined by the relative difference between the lattice constants with and without applied deformation as $\gamma = \frac{c_a - c_0}{c_0} \times 100\%$, where c_a is the strained lattice constant in the *a*-direction, and c_0 is the pristine lattice constant. Positive strain value indicates that tensile strain is applied to the BlueP sheet while the negative one illustrates the level of compression of the material. We applied the strain values in the range of -10% and 10% with a step strain of 2% in the linear elastic regime where the external stress increases linearly with strain (as predicted in [39]).

To understand the orbital modification in a specific bond interaction under deformation in BlueP thin films, we performed the crystal orbital Hamilton population (COHP) method as implemented in the LOBSTER code [54], [55]. This type of analysis helps us to differentiate the types of bonding and antibonding states, which is essential for analyzing the electronic natures of the bonds, especially the strain-induced dangling bonds in our system.

The optical properties of the BlueP thin films were determined by a complex dielectric function $\varepsilon(\omega) = \varepsilon_1(\omega) + i\varepsilon_2(\omega)$, where $\varepsilon_1(\omega)$ and $\varepsilon_2(\omega)$ are the real and imaginary parts of the dielectric function, respectively; and ω is the angular frequency of the incident photon. From the complex dielectric function in the independent approximation for linear optical responses, we can determine the electron energy loss $Im(-\varepsilon^{-1})$, refractive index $n(\omega)$, extinction coefficient $k(\omega)$, reflectivity $R(\omega)$, and absorption coefficient $\alpha(\omega)$ as discussed in detail in the SI.

Acknowledgments

References

[1]   Y. A. Vlasov, X.-Z. Bo, J. C. Sturm, and D. J. Norris, "On-chip natural assembly of silicon photonic bandgap crystals," *Nature*, vol. 414, no. 6861, pp. 289–293, 2001, doi: 10.1038/35104529.

[2]   A.-P. Hynninen, J. H. J. Thijssen, E. C. M. Vermolen, M. Dijkstra, and A. van Blaaderen, "Self-assembly route for photonic crystals with a bandgap in the visible region," *Nat. Mater.*, vol. 6, no. 3, pp. 202–205, 2007, doi: 10.1038/nmat1841.

[3]   T. A. Nguyen, A. Newton, D. J. Kraft, P. G. Bolhuis, and P. Schall, "Tuning Patchy Bonds Induced by Critical Casimir Forces," *Materials (Basel).*, vol. 10, no. 11, 2017, doi: 10.3390/ma10111265.

[4]   K. S. Novoselov, "Electric Field Effect in Atomically Thin Carbon Films," vol. 666, no. 2004, 2012, doi: 10.1126/science.1102896.

[5]   M. P. Levendorf *et al.*, "Graphene and boron nitride lateral heterostructures for atomically thin circuitry," *Nature*, vol. 488, no. 7413, pp. 627–632, 2012, doi: 10.1038/nature11408.

[6] S. Fraser, "Structure of single-molecular-layer MoS2," *Phys. Rev. B*, vol. 43, no. 14, pp. 53–56, 1991.

[7] H. A. Huy, Q. D. Ho, T. Q. Tuan, O. K. Le, and N. Le Hoai Phuong, "Dumbbell configuration of silicon adatom defects on silicene nanoribbons," *Sci. Rep.*, vol. 11, no. 1, p. 14374, 2021, doi: 10.1038/s41598-021-93465-5.

[8] S. Manzeli, D. Ovchinnikov, D. Pasquier, O. V Yazyev, and A. Kis, "2D transition metal dichalcogenides," *Nat. Rev. Mater.*, vol. 2, no. 8, p. 17033, 2017, doi: 10.1038/natrevmats.2017.33.

[9] H. Liu *et al.*, "Phosphorene: An unexplored 2D semiconductor with a high hole mobility," *ACS Nano*, vol. 8, no. 4, pp. 4033–4041, 2014, doi: 10.1021/nn501226z.

[10] P. Srivastava, K. P. S. S. Hembram, H. Mizuseki, K.-R. Lee, S. S. Han, and S. Kim, "Tuning the Electronic and Magnetic Properties of Phosphorene by Vacancies and Adatoms," *J. Phys. Chem. C*, vol. 119, no. 12, pp. 6530–6538, 2015, doi: 10.1021/jp5110938.

[11] G. Yang, Z. Xu, Z. Liu, S. Jin, H. Zhang, and Z. Ding, "Strain- and Fluorination-Induced Quantum Spin Hall Insulators in Blue Phosphorene: A First-Principles Study," *J. Phys. Chem. C*, vol. 121, no. 23, pp. 12945–12952, 2017, doi: 10.1021/acs.jpcc.7b03808.

[12] J. Guan, Z. Zhu, and D. Tománek, "Tiling phosphorene," *ACS Nano*, vol. 8, no. 12, pp. 12763–12768, 2014, doi: 10.1021/nn5059248.

[13] J. Guan, Z. Zhu, and D. Tománek, "Phase coexistence and metal-insulator transition in few-layer phosphorene: A computational study," *Phys. Rev. Lett.*, vol. 113, no. 4, pp. 1–5, 2014, doi: 10.1103/PhysRevLett.113.046804.

[14] H. Zhu, "No-monotonic strain effect on the thermal conductivity of blue phosphorene: A first-principles study," *Phys. E Low-Dimensional Syst. Nanostructures*, vol. 124, no. July, p. 114341, 2020, doi: 10.1016/j.physe.2020.114341.

[15] Z. Zhu and D. Tománek, "Semiconducting layered blue phosphorus: A computational study," *Phys. Rev. Lett.*, vol. 112, no. 17, pp. 1–5, 2014, doi: 10.1103/PhysRevLett.112.176802.

[16] J. L. Zhang *et al.*, "Epitaxial Growth of Single Layer Blue Phosphorus: A New Phase of Two-Dimensional Phosphorus," *Nano Lett.*, vol. 16, no. 8, pp. 4903–4908, 2016, doi: 10.1021/acs.nanolett.6b01459.

[17] W. Zhang *et al.*, "Epitaxial Synthesis of Blue Phosphorene," *Small*, vol. 14, no. 51, pp. 1–6, 2018, doi: 10.1002/smll.201804066.

[18] D. A. Ospina, C. A. Duque, M. E. Mora-Ramos, and J. D. Correa, "Effects of external electric field on the optical and electronic properties of blue phosphorene nanoribbons: A DFT study," *Comput. Mater. Sci.*, vol. 135, pp. 43–53, 2017, doi: 10.1016/j.commatsci.2017.03.048.

[19] G. A. Shaikh, D. Raval, B. Babariya, S. K. Gupta, and P. N. Gajjar, "An ab-initio study of blue phosphorene monolayer: Electronic, vibrational and optical properties," *Mater. Today Proc.*, no. December, pp. 1–5, 2020, doi: 10.1016/j.matpr.2020.10.668.

[20] J. Zhuang *et al.*, "Band Gap Modulated by Electronic Superlattice in Blue Phosphorene," *ACS Nano*, vol. 12, no. 5, pp. 5059–5065, 2018, doi: 10.1021/acsnano.8b02953.

[21] F. Safari, M. Fathipour, and A. Yazdanpanah Goharrizi, "Tuning electronic, magnetic, and transport properties of blue phosphorene by substitutional doping: a first-principles study," *J. Comput. Electron.*, vol. 17, no. 2, pp. 499–513, 2018, doi: 10.1007/s10825-018-1159-z.

[22] K. S. Kim *et al.*, "Large-scale pattern growth of graphene films for stretchable transparent electrodes," *Nature*, vol. 457, no. 7230, pp. 706–710, 2009, doi: 10.1038/nature07719.

[23] C. Lee, X. Wei, J. W. Kysar, and J. Hone, "Measurement of the Elastic Properties and

Intrinsic Strength of Monolayer Graphene," *Science (80-.).*, vol. 321, no. 5887, pp. 385–388, 2008, doi: 10.1126/science.1157996.

[24] X. Peng, Q. Wei, and A. Copple, "Strain-engineered direct-indirect band gap transition and its mechanism in two-dimensional phosphorene," *Phys. Rev. B*, vol. 90, no. 8, p. 85402, Aug. 2014, doi: 10.1103/PhysRevB.90.085402.

[25] X. Liu *et al.*, "2D phosphorene nanosheets, quantum dots, nanoribbons: synthesis and biomedical applications," *Biomater. Sci.*, vol. 9, no. 8, pp. 2768–2803, 2021, doi: 10.1039/D0BM01972K.

[26] R. Ghaffari, F. Shirazian, M. Hu, and R. A. Sauer, "A nonlinear hyperelasticity model for single layer blue phosphorus based on *ab initio* calculations," *Proc. R. Soc. A Math. Phys. Eng. Sci.*, vol. 475, no. 2229, p. 20190149, 2019, doi: 10.1098/rspa.2019.0149.

[27] A. S. Rodin, A. Carvalho, and A. H. Castro Neto, "Strain-Induced Gap Modification in Black Phosphorus," *Phys. Rev. Lett.*, vol. 112, no. 17, p. 176801, May 2014, doi: 10.1103/PhysRevLett.112.176801.

[28] Y. Aierken, D. Cakir, C. Sevik, and F. M. Peeters, "Thermal properties of black and blue phosphorenes from a first-principles quasiharmonic approach," *Phys. Rev. B*, vol. 92, no. 8, p. 81408, Aug. 2015, doi: 10.1103/PhysRevB.92.081408.

[29] J. Xie, M. S. Si, D. Z. Yang, Z. Y. Zhang, and D. S. Xue, "A theoretical study of blue phosphorene nanoribbons based on first-principles calculations," *J. Appl. Phys.*, vol. 116, no. 7, p. 73704, 2014, doi: 10.1063/1.4893589.

[30] F. Iyikanat, E. Torun, R. T. Senger, and H. Sahin, "Stacking-dependent excitonic properties of bilayer blue phosphorene," *Phys. Rev. B*, vol. 100, no. 12, p. 125423, Sep. 2019, doi: 10.1103/PhysRevB.100.125423.

[31] Y. Lu, G. Xiao, Y. Wang, M. Gao, and Z. Chen, "First-principles study on the influence of biaxial strain on the electronic and magnetic properties of defective blue phosphorene," *Phys. Lett. A*, vol. 384, no. 35, p. 126853, 2020, doi: https://doi.org/10.1016/j.physleta.2020.126853.

[32] M. Sun, J.-P. Chou, A. Hu, and U. Schwingenschlögl, "Point Defects in Blue Phosphorene," *Chem. Mater.*, vol. 31, no. 19, pp. 8129–8135, 2019, doi: 10.1021/acs.chemmater.9b02871.

[33] S. V Boriskina, J. Zhou, Z. Ding, and G. Chen, "Efficiency Limits of Solar Energy Harvesting via Internal Photoemission in Carbon Materials," *Photonics*, vol. 5, no. 1, 2018, doi: 10.3390/photonics5010004.

[34] S. Chintalapati, L. Shen, Q. Xiong, and Y. P. Feng, "Magnetism in phosphorene: Interplay between vacancy and strain," *Appl. Phys. Lett.*, vol. 107, no. 7, p. 72401, 2015, doi: 10.1063/1.4928754.

[35] V. Chikkadi, D. M. Miedema, M. T. Dang, B. Nienhuis, and P. Schall, "Shear banding of colloidal glasses: Observation of a dynamic first-order transition," *Phys. Rev. Lett.*, vol. 113, no. 20, pp. 1–5, 2014, doi: 10.1103/PhysRevLett.113.208301.

[36] M. T. Dang, R. Zargar, D. Bonn, A. Zaccone, and P. Schall, "Nonequilibrium free energy of colloidal glasses under shear," *J. Phys. D. Appl. Phys.*, vol. 51, no. 32, p. 324002, Jul. 2018, doi: 10.1088/1361-6463/aad03a.

[37] D. Denisov, M. T. Dang, B. Struth, G. Wegdam, and P. Schall, "Resolving structural modifications of colloidal glasses by combining x-ray scattering and rheology," *Sci. Rep.*, vol. 3, no. 1, p. 1631, 2013, doi: 10.1038/srep01631.

[38] D. V Denisov, M. T. Dang, B. Struth, A. Zaccone, G. H. Wegdam, and P. Schall, "Sharp symmetry-change marks the mechanical failure transition of glasses," *Sci. Rep.*, vol. 5, pp.

14359--, Sep. 2015, [Online]. Available: http://dx.doi.org/10.1038/srep14359.

[39] R. Swaroop, P. K. Ahluwalia, K. Tankeshwar, and A. Kumar, "Ultra-narrow blue phosphorene nanoribbons for tunable optoelectronics," *RSC Adv.*, vol. 7, no. 5, pp. 2992–3002, 2017, doi: 10.1039/C6RA26253H.

[40] D. R. Penn, "Wave-Number-Dependent Dielectric Function of Semiconductors," *Phys. Rev.*, vol. 128, no. 5, pp. 2093–2097, Dec. 1962, doi: 10.1103/PhysRev.128.2093.

[41] M. Quinten, *Optical Properties of Nanoparticle Systems: Mie and beyond.* 2011.

[42] L. Shulenburger, A. D. Baczewski, Z. Zhu, J. Guan, and D. Tománek, "The Nature of the Interlayer Interaction in Bulk and Few-Layer Phosphorus," *Nano Lett.*, vol. 15, no. 12, pp. 8170–8175, Dec. 2015, doi: 10.1021/acs.nanolett.5b03615.

[43] A. Zaccone and E. M. Terentjev, "Disorder-assisted melting and the glass transition in amorphous solids," *Phys. Rev. Lett*, vol. 110, no. 17, p. 178002, 2013.

[44] J. K. G. Dhont, *An Introduction to Dynamics of Colloids.* Elsevier, Amsterdam, 1996.

[45] A. Zaccone, P. Schall, and E. M. Terentjev, "Microscopic origin of nonlinear nonaffine deformation in bulk metallic glasses," *Phys. Rev. B*, vol. 90, no. 14, p. 140203, Oct. 2014, doi: 10.1103/PhysRevB.90.140203.

[46] M. Laurati, P. Ma\sshoff, K. J. Mutch, S. U. Egelhaaf, and A. Zaccone, "Long-Lived Neighbors Determine the Rheological Response of Glasses," *Phys. Rev. Lett.*, vol. 118, no. 1, p. 18002, Jan. 2017, doi: 10.1103/PhysRevLett.118.018002.

[47] H. He and M. F. Thorpe, "Elastic Properties of Glasses," *Phys. Rev. Lett.*, vol. 54, no. 19, pp. 2107–2110, May 1985, doi: 10.1103/PhysRevLett.54.2107.

[48] C. Zener, *Elasticity and Anelasticity of Metals.* Chicago Univ. Press, Chicago, 1965.

[49] G. Kresse and J. Hafner, "Ab initio molecular-dynamics simulation of the liquid-metal--amorphous-semiconductor transition in germanium," *Phys. Rev. B*, vol. 49, no. 20, pp. 14251–14269, May 1994, doi: 10.1103/PhysRevB.49.14251.

[50] G. Kresse and D. Joubert, "From ultrasoft pseudopotentials to the projector augmented-wave method," *Phys. Rev. B*, vol. 59, no. 3, pp. 1758–1775, Jan. 1999, doi: 10.1103/PhysRevB.59.1758.

[51] G. Kresse and J. Furthmüller, "Efficiency of ab-initio total energy calculations for metals and semiconductors using a plane-wave basis set," *Comput. Mater. Sci.*, vol. 6, no. 1, pp. 15–50, 1996, doi: https://doi.org/10.1016/0927-0256(96)00008-0.

[52] J. P. Perdew, K. Burke, and M. Ernzerhof, "Generalized Gradient Approximation Made Simple," *Phys. Rev. Lett.*, vol. 77, no. 18, pp. 3865–3868, Oct. 1996, doi: 10.1103/PhysRevLett.77.3865.

[53] H. J. Monkhorst and J. D. Pack, "Special points for Brillouin-zone integrations," *Phys. Rev. B*, vol. 13, no. 12, pp. 5188–5192, Jun. 1976, doi: 10.1103/PhysRevB.13.5188.

[54] V. L. Deringer, A. L. Tchougréeff, and R. Dronskowski, "Crystal Orbital Hamilton Population (COHP) Analysis As Projected from Plane-Wave Basis Sets," *J. Phys. Chem. A*, vol. 115, no. 21, pp. 5461–5466, 2011, doi: 10.1021/jp202489s.

[55] S. Maintz, V. L. Deringer, A. L. Tchougréeff, and R. Dronskowski, "Analytic projection from plane-wave and PAW wavefunctions and application to chemical-bonding analysis in solids," *J. Comput. Chem.*, vol. 34, no. 29, pp. 2557–2567, 2013, doi: https://doi.org/10.1002/jcc.23424.
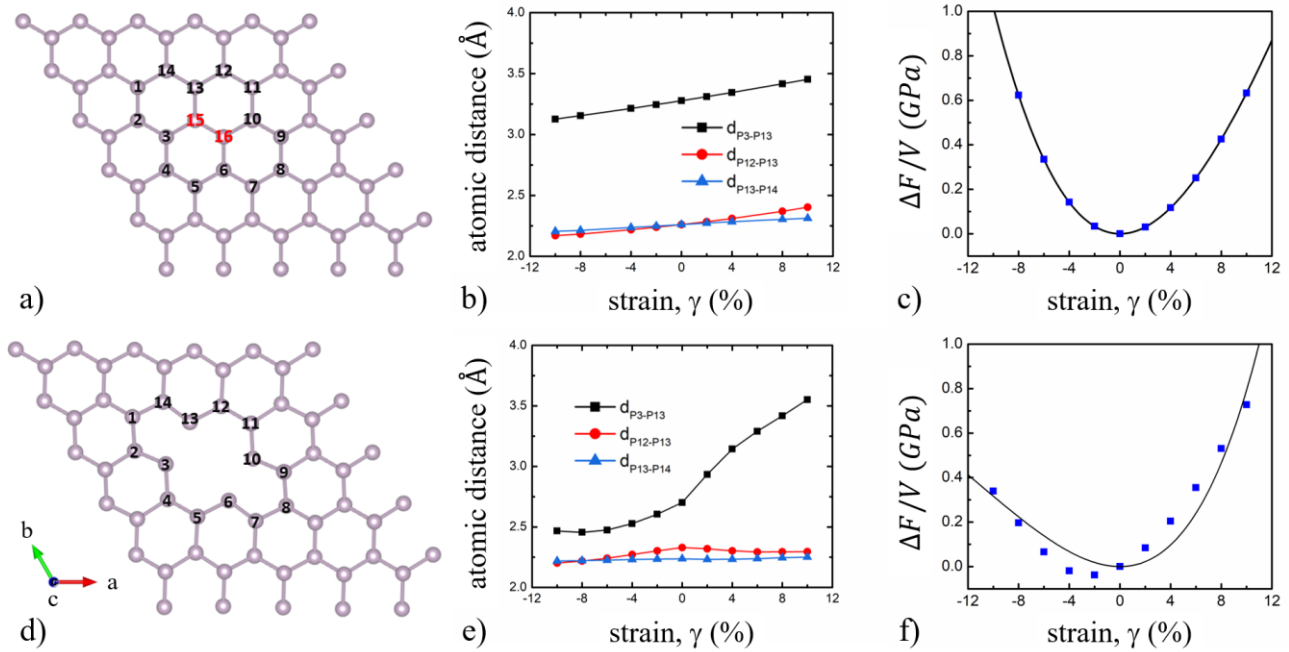
Figure 1. **Optimized configurations, selected atomic distances and free energy density changes of pristine and DV BlueP under deformation.** The optimized configurations of (a) pristine BlueP and (d) DV BlueP at zero strain. Atomic distance variation of pristine (b) and DV (e) BlueP under compressive (negative) and tensile (positive) deformations. A linear increase of atomic distances with strains highlights an affine deformation of pristine BlueP while a non-monotonic behavior of atomic distances versus strains suggests a major contribution of non-affinity in DV BlueP. Free energy density difference between the strained and unstrained states of pristine (c) and DV (f) BlueP as a function of strain (blue squares are simulation data and black curves indicate the fits according to our microscopic affine-(non-)affine model).
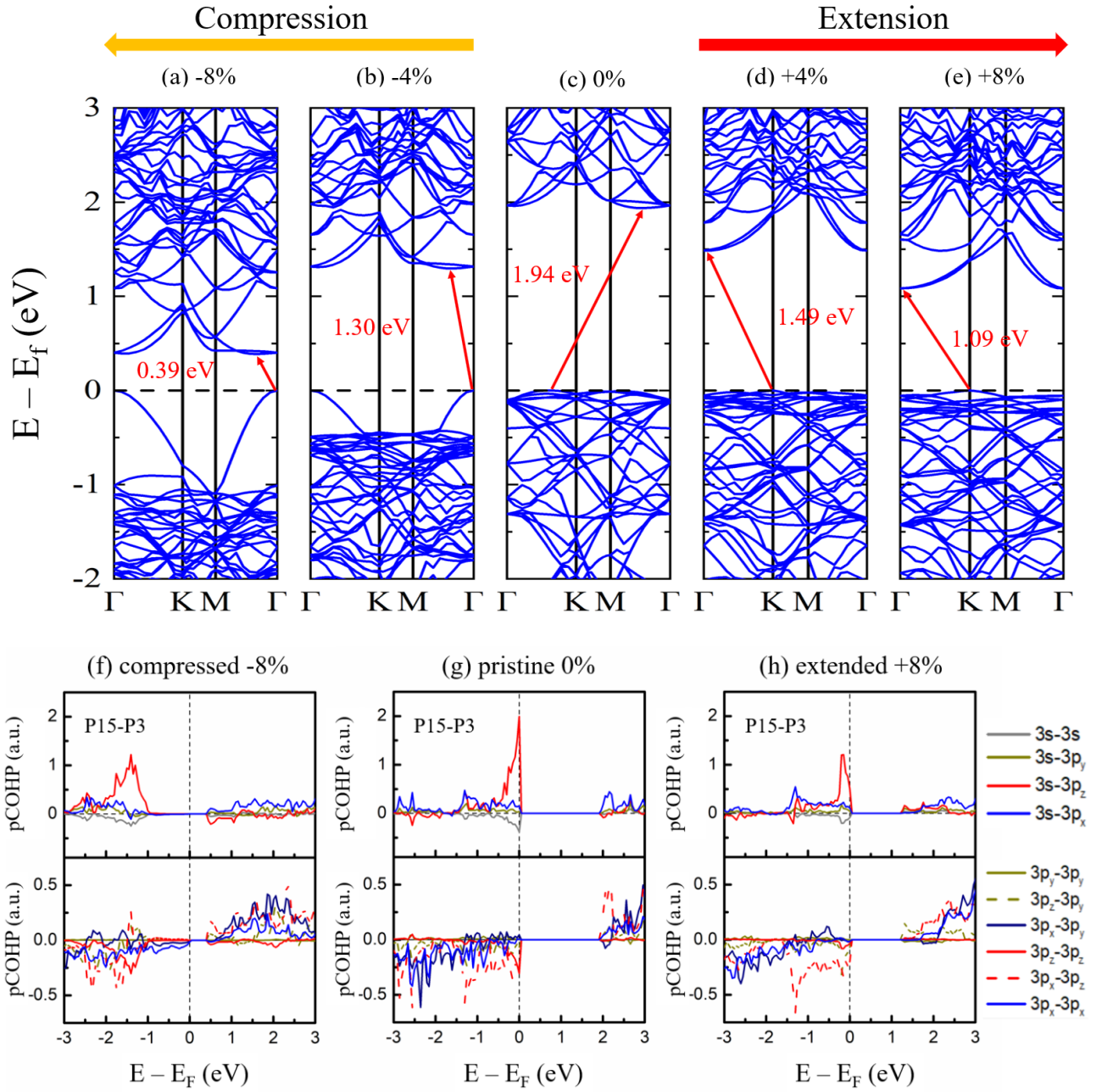
Figure 2. Band structures and P15-P3 projected crystal overlap Hamilton population (pCOHP) of pristine BlueP under deformation in the *a*-direction. The red arrows illustrate the positions of VBM and CBM. The Fermi level indicated by black dash lines is set to zero.
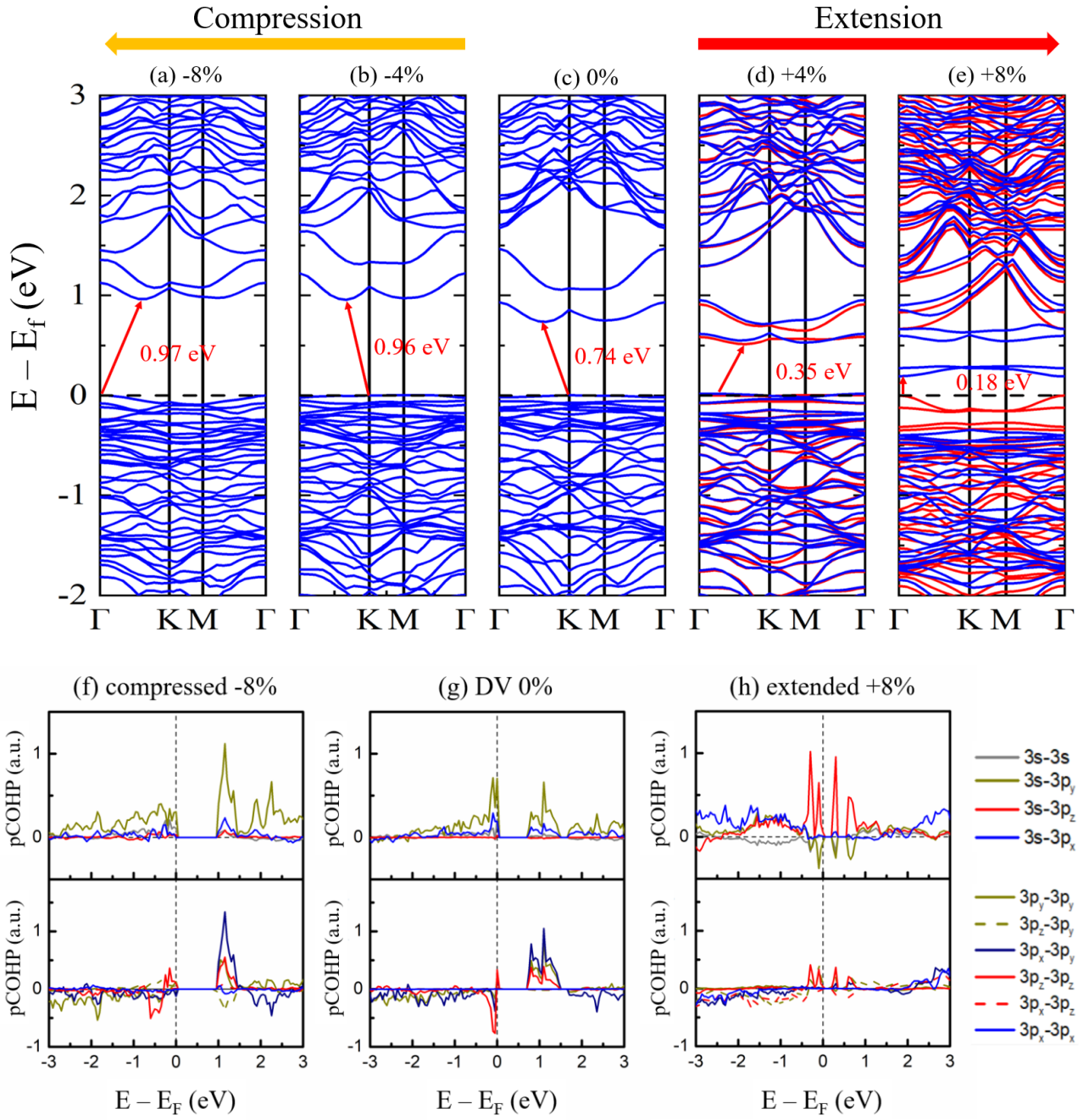
Figure 3. Band structures and P3-P13 projected crystal overlap Hamilton population (pCOHP) of DV BlueP under deformation in the *a*-direction. The red (blue) lines in the band structures represent spin-up (spin-down) bands. The red arrows illustrate the positions of VBM and CBM. The Fermi level indicated by black dash lines is set to zero.
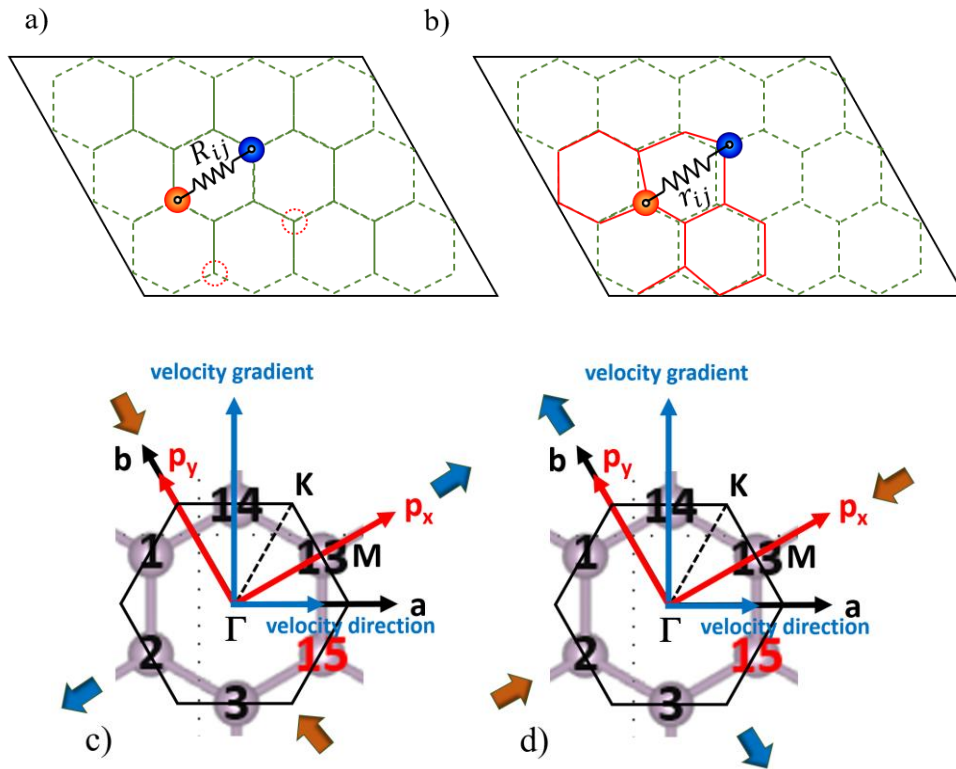
Figure 4. Sketches of affine (a) and non-affine (b) deformations of a pristine BlueP and sketches of a Brillouin zone together a directional distortion of nearest-neighbors under tensile (c) and compressive (d) deformation. In a perfect BlueP system (a), the net force acting on a P atom is cancelled by symmetry, while in a non-perfect BlueP solid (b), the non-zero affine net force acting on a P atom has to be balanced by non-affine motion created by the surrounding P network. The model here assumes a pristine BlueP is under a tensile strain.
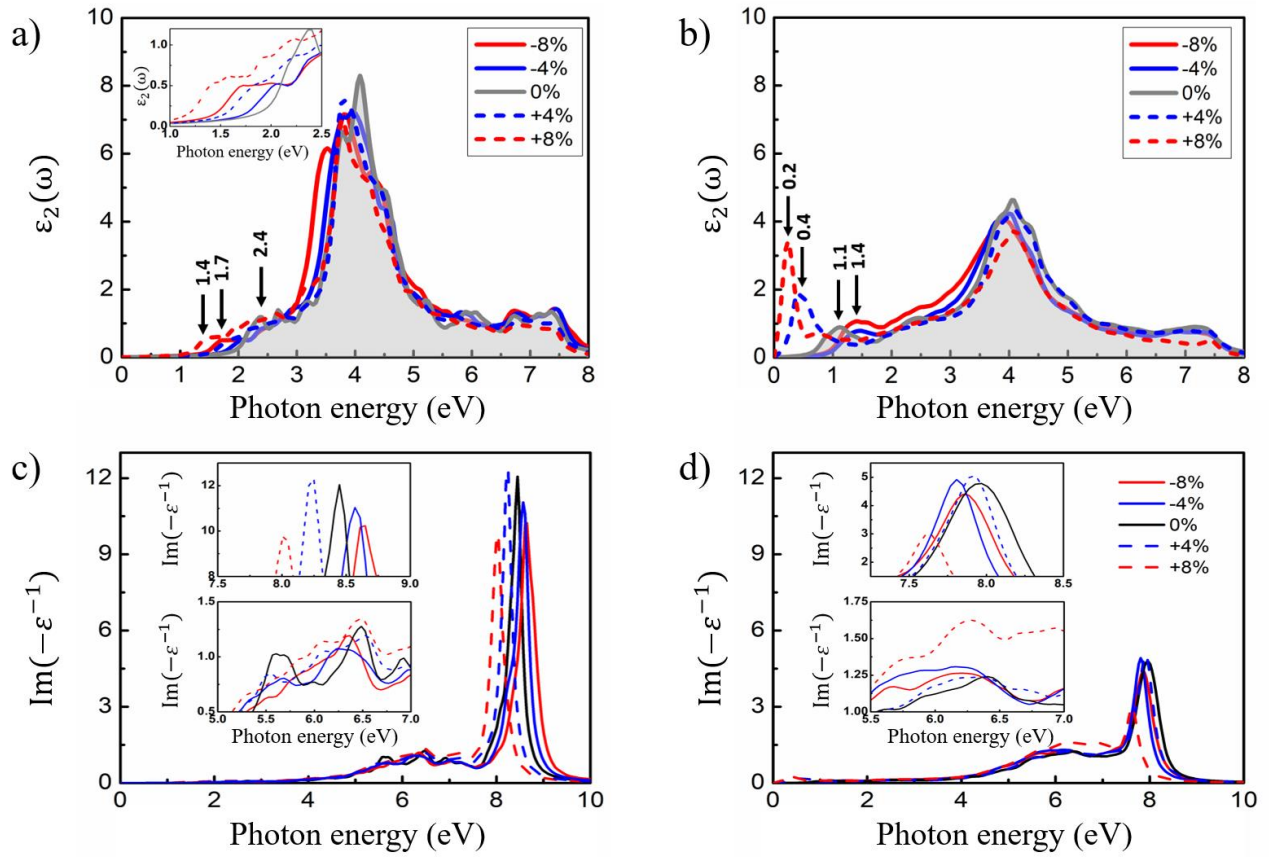
Figure 5. The imaginary parts of the dielectric functions and electron energy loss (EEL) spectra of pristine and DV BlueP under deformation in the *a*-direction. Values with arrows in (a) and (b) indicate the first dominant peaks of the imaginary parts at certain strains. The upper insets in (c) and (d) illustrate the EEL spectra of $\sigma + \pi$ plasmons while the lower insets in these figures show the σ plasmon spectra.

	κ (Nm^{-1})	G_R (Nm^{-1})	G (Nm^{-1})	ν
pristine	76.28 (75.85)	30 (30.94)	52.34 (48.98)	0.271 (0.226)
divacancy	61.43	23.98	42.71	0.281

Table 1. Young's modulus (κ), shear modulus (G_R), bulk modulus (G), Poisson's ratio (ν) of pristine and DV BlueP under deformation. The values in brackets are taken from [26].

Strain (%)	Dielectric constant		Refractive index		Reflectivity	
	pristine	DV	pristine	DV	pristine	DV
-8	3.27	2.98	1.81	1.76	0.082	0.070
-4	3.07	2.74	1.75	1.66	0.074	0.060
0	2.99	2.95	1.73	1.72	0.071	0.069
4	2.95	3.99	1.72	1.99	0.069	0.110
8	3.03	5.78	1.74	2.40	0.073	0.170

Table 2. Optical constants of pristine and DV BlueP under deformation in the *a*-direction. These optical constants are obtained at the zero photon frequency.

Strain (%)	E_g (eV)		E_P(eV) from Penn's model		E_P (eV) from $|\varepsilon|$	
	pristine	DV	pristine	DV	pristine	DV
-8	0.39	0.97	0.58	1.36	-	1.16
-4	1.23	0.96	1.87	1.26	1.96	1.16
0	1.94	0.73	2.73	1.03	2.60	0.80
4	1.45	0.35	2.08	0.60	2.08	0.32
8	1.09	0.18	1.55	0.38	1.32	0.16

Table 3. Comparison of plasmonic energy (E_P) from Penn's model expression and from the module of the complex dielectric constant. The electronic band gaps (E_g) are obtained from the difference between the valence band maximum and the conduction band minimum.